FRONTIERS OF PHYSICS

RESEARCH ARTICLE
Volume 22 / Issue 4 / 044202 / 2027

# Classical device modelling of grain size and boundary effects on the performance of $CsSnI_3$ polycrystalline perovskite solar cells

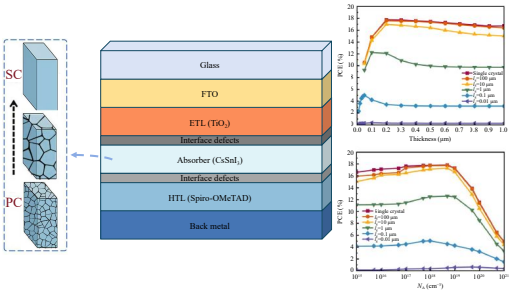
Run Wang[1], Baoping Zhang[2], Huanting Chen[1], Cuiyong Tang[3], Chuanjin Lin[1], Jinhai Liu[1], Huaqing Pan[4], Kaizhi Li[1], Shuo Lin[1,†], Jincheng Zheng[5,6,‡]

1 Optoelectronic Materials & Device Application Industry Technological Development Base of Fujian Province, School of Physics and Information Engineering, Minnan Normal University, Zhangzhou 363000, China
2 Institute of Nanoscience and Applications, Southern University of Science and Technology, Shenzhen 518055, China
3 College of Mechanical and Electrical Engineering, Fujian Agriculture and Forestry University, Fuzhou 350100, China
4 Department of Mechanical Engineering, Shangrao Vocational and Technical College, Shangrao 334109, China
5 Collaborative Innovation Center for Optoelectronic Semiconductors and Efficient Devices, Department of Physics, Xiamen University, Xiamen 361005, China
6 Department of Physics and Department of New Energy Science and Engineering, Xiamen University Malaysia, Sepang 43900, Selangor, Malaysia
Corresponding authors. E-mail: †linshuo_pv@163.com, ‡jczheng@xmu.edu.cn
Received August 10, 2026; accepted October 15, 2026

© Higher Education Press 2027

## ABSTRACT

In this study we systematically investigate the influence of grain size on the performance of lead-free $CsSnI_3$ perovskite solar cells and the underlying physical mechanisms. Using a weighted-average approach, we calculate the electron and hole mobilities as functions of grain size, and develop a grain-boundary defect model based on the Matthiessen rule to establish a quantitative correlation between grain size and defect density. These extracted mobility and defect parameters are then imported into SCAPS-1D to construct a $TiO_2$/$CsSnI_3$/Spiro-OMeTAD planar heterojunction device, enabling a comprehensive analysis of how grain size modulates the optimization of absorber thickness, doping concentration, and interface defect tolerance. Our results show that enlarging grain size significantly enhances carrier mobility and reduces defect density, thereby effectively suppressing non-radiative recombination and improving charge extraction efficiency. The maximum power conversion efficiency (PCE) decreases from 17.82% for single-crystalline $CsSnI_3$ to 17.75%, 17.29, 12.59, 5.06, and 0.65% for grain sizes of 100, 10, 1, 0.1, and 0.01 μm, respectively. Devices with larger grains exhibit greater tolerance to both thicker absorbers and interface defects, whereas their smaller-grain counterparts suffer from pronounced recombination losses and heightened parametric sensitivity. Notably, defects at the electron transport layer (ETL) /$CsSnI_3$ interface are found to have a more detrimental effect on device performance than those at the $CsSnI_3$/hole transport layer (HTL) interface. Overall, this work elucidates the intrinsic mechanisms by which grain size governs $CsSnI_3$ device performance, providing a theoretical basis for the structural optimization of high-performance lead-free perovskite photovoltaics.




Higher Education Press

https://doi.org/10.15302/frontphys.2027.044202

**Keywords** perovskite solar cells, $CsSnI_3$ polycrystalline perovskites, grain size, device simulation

## 1 Introduction

In recent years, perovskite solar cells (PSCs) have attracted widespread attention due to their outstanding optoelectronic properties. Over the past decade, the power conversion efficiency (PCE) of PSCs has undergone a remarkable leap, rising rapidly from an initial 14.1% to 28% [1], as shown in Fig. 1, demonstrating substantial commercial potential. Nevertheless, their large-scale commercialization still faces technical bottlenecks including system integration, interface management and patterned manufacturing [2].

Currently, high-performance PSCs predominantly employ lead-containing perovskite materials, such as $MAPbI_3$, $FAPbI_3$, and their mixed systems [3]. However, the toxicity of lead remains a significant obstacle limiting the large-scale commercialization of PSCs. During device fabrication, operation, and disposal, lead leakage can pose severe risks to the ecological environment and human health [4]. Furthermore, perovskite materials themselves are sensitive to moisture, oxygen, heat, and light. Their stability issues further exacerbate the risk of lead contamination [5]. Therefore, developing lead-free perovskite materials that are highly efficient, low-toxicity, and environmentally friendly has become a critical research direction.

Tin-based perovskites, where Sn belongs to the same group IVA as Pb and shares a similar electronic configuration, are considered among the most promising lead-free alternatives [6]. Among them, the all-inorganic perovskite $CsSnI_3$ has attracted extensive attention due to its excellent optoelectronic properties. $CsSnI_3$ possesses a direct bandgap of approximately 1.3 eV, which is close to the optimal bandgap range for the Shockley–Queisser theoretical limit, enabling efficient sunlight absorption [7]. Moreover, $CsSnI_3$ exhibits a high absorption coefficient (on the order of $10^4$ $cm^{-1}$ in the visible region), allowing sufficient light absorption even with a thin absorber layer, thereby reducing material consumption and improving carrier collection efficiency [8]. Furthermore, $CsSnI_3$ demonstrates superior charge-carrier transport properties, with a hole mobility as high as ~ 400–585 $cm^2/(V{\cdot}s)$ [9], which is among the highest values observed for p-type semiconductors with comparable band gaps. In addition, $CsSnI_3$ features a low exciton binding energy of approximately 10–20 meV (Wannier-type excitons), facilitating more efficient exciton dissociation and carrier separation compared to typical organic absorbers. Compared with organic–inorganic hybrid perovskites, all-inorganic $CsSnI_3$ also offers clear advantages in thermal stability [10], making long-term stable operation feasible. In recent years, significant progress has been made in the study of $CsSnI_3$ PSCs. The highest reported laboratory PCE has reached 14.95% [11], as also shown in Fig. 1. This underscores that this field is entering a period of rapid development.

Although $CsSnI_3$ shows promising application potential, its device performance remains significantly lower than that of lead-based perovskite systems [12]. Because of the low formation energy of Sn vacancies ($V_{Sn}$), they are readily formed during material growth, leading to severe spontaneous p-type doping and a large number of deep-level trap states [13]. These defects significantly enhance the Shockley–Read–Hall (SRH) non-radiative recombination process, shortening carrier lifetime and reducing the open-circuit voltage ($V_{OC}$). In addition, $Sn^{2+}$ is prone to oxidation to $Sn^{4+}$, which further introduces additional defect states and degrades both material stability and device performance [14]. Sn-rich conditions in $CsSnI_3$ nanoplatelets have been demonstrated to reduce defect density and improve stability [15]. This performance regulation strategy via defect engineering has been widely validated in functional material fields such as thermoelectrics and luminescence [16, 17].

Beyond intrinsic defects, $CsSnI_3$ thin films also typically possess pronounced polycrystalline features. In practice, perovskite films are composed of numerous grains with heterogeneous sizes, and the grain boundaries (GBs) between adjacent grains are widely recognized as regions of elevated defect density [18]. These GBs not only intensify carrier scattering but also introduce a substantial population of trap states, which facilitate interfacial recombination and consequently degrade both carrier mobility and diffusion length [19]. As such, grain size has emerged as a critical microstructural parameter governing the overall performance of perovskite-based devices. In addition, crystal plane surface termination, intergranular secondary phases, heterojunction interfacial defects, and crystallization orientation/phase separation behavior of low-dimensional perovskites also significantly affect the device output of polycrystalline systems [20–23].

Previous studies [24–27] have shown that increasing grain size can effectively reduce the number of grain boundaries, lower recombination losses, and improve device efficiency. However, current research on polycrystalline $CsSnI_3$ systems remains largely focused on experimental fabrication process optimization, such as solvent engineering, additive regulation, surface passivation, and interface modification [18, 26, 28–30]. Systematic investigations into how grain size simultaneously affects carrier mobility, defect density, and key device parameters

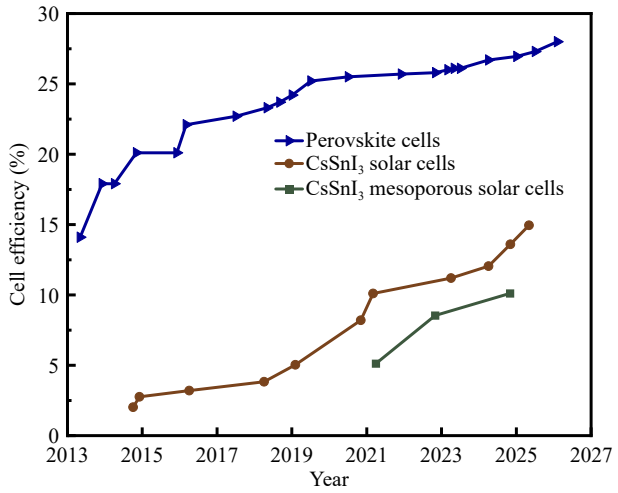



**Fig. 1** Historical evolution of the record power conversion efficiencies (PCEs) of PSCs and $CsSnI_3$-based lead-free perovskite solar cells reported between 2013 and 2026 [1, 11]. The blue, brown, and green curves represent lead-halide PSCs, conventional $CsSnI_3$ solar cells, and mesoporous $CsSnI_3$ solar cells, respectively. While lead-based PSCs have achieved efficiencies approaching 28%, $CsSnI_3$ devices have reached only about 15%. The consistently lower efficiencies of mesoporous $CsSnI_3$ devices are generally attributed to the porous scaffold, which creates abundant grain boundaries and defect states, thereby increasing nonradiative carrier recombination and hindering efficient charge transport.

(e.g., absorber layer thickness, doping concentration, and tolerance to interface defects) remain relatively limited. In particular, variations in grain size typically alter both mobility and defect characteristics simultaneously, and their coupled effects on device performance mean that the underlying physical mechanisms have yet to be fully elucidated. For simulation methods, emerging technologies such as machine learning force fields and data-driven modeling can provide methodological references for polycrystalline perovskite device simulation [31–33]; simulation studies on lead-free quasi-2D/2D bilayer structures have also confirmed the optimization effect of layered band structures on carrier transport [34]. Furthermore, to the best of our knowledge, there has been no literature on the simulation study of polycrystalline effects in $CsSnI_3$ solar cells so far.

To address this gap, the present study integrates theoretical modeling with numerical simulation to systematically explore the performance evolution of $CsSnI_3$ PSCs as a function of grain size. First, the weighted average method (WAM) is adopted to evaluate the electron and hole mobilities corresponding to various grain sizes, while a grain boundary defect model is developed based on the Matthiessen rule to establish a quantitative correlation between grain size and defect density. Subsequently, the extracted mobility and defect density parameters are fed into the SCAPS-1D (Solar Cell Capacitance Simulator) to construct a $TiO_2/CsSnI_3$/Spiro-OMeTAD planar heterojunction solar cell. This enables a comprehensive analysis of how grain size governs the optimization of absorber layer thickness, the regulation of doping concentration, and the influence of interfacial defects. Overall, this work not only elucidates the intrinsic mechanisms through which grain size modulates the photovoltaic performance of $CsSnI_3$ solar cells but also furnishes a theoretical foundation for the structural design of high-performance lead-free PSCs.

## 2 Theoretical methods and computational model

### 2.1 SCAPS simulation software

In this work, the solar cell capacitance simulator SCAPS-1D is employed to numerically simulate $CsSnI_3$ PSCs. SCAPS-1D is a one-dimensional solar cell simulation software based on the drift-diffusion model, developed at the University of Ghent, Belgium [35–37], and is widely used for theoretical investigations and performance optimization of thin-film solar cells and PSCs.

SCAPS-1D self-consistently calculates the internal band diagram, electric field distribution, carrier transport behavior, and recombination dynamics within the device by solving the Poisson equation [Eq. (1)] along with the continuity equations for electrons [Eq. (2)] and holes [Eq. (3)] [35, 38–41]. It thereby yields the current density–voltage ($J$–$V$) characteristics, quantum efficiency, and key performance parameters, including $V_{OC}$, short-circuit current density ($J_{SC}$), fill factor (FF), and PCE [42]. The governing equations are presented as follows:

Poisson equation:

$$\frac{\mathrm{d}^2}{\mathrm{d}x^2}\Psi(x) = \frac{e}{\varepsilon_0\varepsilon_r}\left[p(x) + N_D + \rho_p - n(x) - N_A - \rho_n\right]; \tag{1}$$

Continuity equation for electrons:

$$-\frac{1}{q}\frac{\mathrm{d}J_n(x)}{\mathrm{d}x} = G(x) - R(x); \tag{2}$$

Continuity equation for holes:

$$\frac{1}{q}\frac{\mathrm{d}J_p(x)}{\mathrm{d}x} = G(x) - R(x), \tag{3}$$

where $\Psi$ is the electrostatic potential distribution, $\varepsilon_0$ is the vacuum permittivity, $\varepsilon_r$ is the relative permittivity, $N_D$ and $N_A$ denote the donor and acceptor densities, respectively, and $\rho_p$ and $\rho_n$ represent the hole and electron distributions, respectively. $J_n$ and $J_p$ are the electron and hole current densities, respectively, while $G(x)$ and

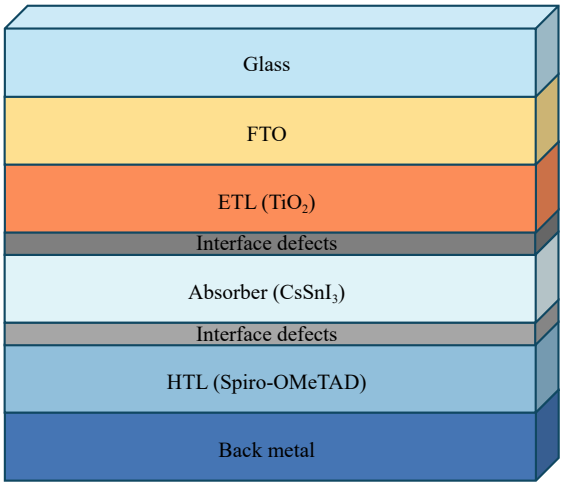



**Fig. 2** Configuration of the $CsSnI_3$ solar cell structure.

$R(x)$ denote the carrier generation rate and the electron–hole recombination rate, respectively.

Compared with experimental investigations, SCAPS numerical simulation offers advantages such as low cost, controllable variables, and the ability to independently analyze the influence of a single factor, making it particularly suitable for studying the impact of grain size variation on the internal physical processes of polycrystalline perovskite devices. Therefore, this work employs SCAPS to systematically investigate the performance variation of $CsSnI_3$ solar cells under different grain sizes.

### 2.2 Device structure and parameter settings

Simulations are performed under standard test conditions: AM1.5G spectrum, an incident light power density of 100 $mW{\cdot}cm^{-2}$, and an operating temperature of 300 K. The device adopts a planar heterojunction structure, consisting of a transparent conductive oxide front electrode (FTO), an electron transport layer ($TiO_2$), a $CsSnI_3$ perovskite light-absorbing layer, a hole transport layer (Spiro-OMeTAD), and a back electrode stacked in sequence. A schematic diagram of the device geometry is shown in Fig. 2.

The key material parameters required for the simulations are summarized in Table 1, including the thickness, relative permittivity, bandgap, electron affinity, effective densities of states in the conduction and valence bands, carrier mobility, donor/acceptor doping concentration, and bulk defect density for each layer. These parameters are primarily derived from experimental and theoretical results reported in the literature [9, 24, 43]. Notably, in the initial simulations, no additional interface defect states are introduced at the heterojunction interfaces, which are consequently assumed to be ideal contacts. This approach is adopted to first establish a baseline performance benchmark for $CsSnI_3$-based devices, thereby enabling a more unambiguous assessment of the influence exerted by the absorber layer's intrinsic parameters on device performance. In subsequent optimization stages, interface defects will be progressively incorporated to evaluate their effects. Meanwhile, the radiative recombination coefficient of $CsSnI_3$ is set to $1 \times 10^{-10}$ $cm^3{\cdot}s^{-1}$ [44]. Additionally, parasitic optical absorption in the ETL $TiO_2$ and HTL Spiro is neglected.

### 2.3 Defect density model (based on the Matthiessen rule)

In polycrystalline PSCs, grain boundaries are the primary sites for defect accumulation, carrier recombination, and device degradation. The overall defect state density of the polycrystalline system is governed by two key factors: grain size and grain boundary defect density [19]. Following the classical modeling approach for carrier lifetime and defect density in polycrystalline perovskites, the Matthiessen rule serves as the fundamental principle for describing the superposition of multiple scattering and recombination processes in polycrystalline semiconductors. Its core premise is that the total decay rate of a polycrystalline system is the linear sum of the intrinsic decay rate of the corresponding single crystal

**Table 1** Physical parameters used for simulations [9, 24, 43].

| Parameters | $TiO_2$ | $CsSnI_3$ | Spiro-OMeTAD |
|---|---|---|---|
| Thickness (nm) | 30 | 200 | 200 |
| $E_g$ (eV) | 3.2 | 1.3 | 3.06 |
| $X$ (eV) | 4.1 | 3.62 | 2.05 |
| $\varepsilon_r$ | 55 | 48.2 | 3 |
| $N_C$ ($cm^{-3}$) | $1 \times 10^{21}$ | $1.57 \times 10^{19}$ | $1 \times 10^{19}$ |
| $N_V$ ($cm^{-3}$) | $2 \times 10^{20}$ | $1.47 \times 10^{18}$ | $1 \times 10^{19}$ |
| $\mu_n$ ($cm^2{\cdot}V^{-1}{\cdot}s^{-1}$) | 0.006 | 50 | $2 \times 10^{-4}$ |
| $\mu_p$ ($cm^2{\cdot}V^{-1}{\cdot}s^{-1}$) | 0.006 | 585 | $2 \times 10^{-4}$ |
| $N_A$ ($cm^{-3}$) | 0 | $5 \times 10^{17}$ | $1 \times 10^{18}$ |
| $N_D$ ($cm^{-3}$) | $1 \times 10^{21}$ | 0 | 0 |
| $N_t$ ($cm^{-3}$) | | $1 \times 10^{13}$ | |

and the decay rate contributed by grain boundaries [35, 45]. At the carrier recombination level, the SRH recombination lifetime of carriers in polycrystalline $CsSnI_3$ perovskite follows the Matthiessen rule [46–48]:

$$\frac{1}{\tau_{poly}} = \frac{1}{\tau_{mono}} + \frac{1}{\tau_{gb}}, \tag{4}$$

where $\tau_{poly}$ is the effective carrier recombination lifetime of polycrystalline $CsSnI_3$, $\tau_{mono}$ is the intrinsic recombination lifetime of single-crystal $CsSnI_3$, and $\tau_{gb}$ is the carrier recombination lifetime induced by grain boundaries. In semiconductors, the SRH defect-assisted recombination lifetime and the defect density satisfy the classical relationship [49, 50]:

$$\tau_{poly(mono)} = \frac{1}{\sigma_{poly(mono)} V_{th} N_{poly(mono)}}, \tag{5}$$

where $N$ is the defect density, $V_{th}$ is the thermal velocity of carriers, and $\sigma$ is the carrier capture cross-section. The recombination lifetime at grain boundaries can be characterized by the grain size and the grain boundary surface recombination properties [49, 50]:

$$\tau_{gb} = \frac{l_g}{S_{gb}} = \frac{l_g}{\sigma_{mono} V_{th} N_{gb}}, \tag{6}$$

where $l_g$ is the grain size, $N_{gb}$ is the grain boundary interface defect density, and $S_{gb}$ is the grain boundary surface recombination velocity. By substituting the lifetime–defect density relationships into the Matthiessen lifetime superposition formula and simultaneously eliminating the carrier thermal velocity $V_{th}$ and the capture cross-section $\sigma$, the theoretical expression for the bulk defect density $N_{poly}$ of polycrystalline $CsSnI_3$ can be derived.

Based on the simplified classical perovskite defect model, with the $CsSnI_3$-specific bandgap redshift correction and linear defect contributions from grains and grain boundaries, the core defect density model is simplified as [51]

$$N_{poly} = N_{mono} + \frac{N_{gb}}{l_g}, \tag{7}$$

where $N_{mono}$ is an effective single-crystal reference defect density, representing an idealized low-defect limit. A value of $1 \times 10^{13}$ $cm^{-3}$ has been widely adopted in SCAPS-1D simulations of $CsSnI_3$ and related perovskite devices [52–55]. It should be noted that defect densities for $CsSnI_3$ single crystals depend strongly on growth method, purity, and measurement technique, and no universally accepted direct value has been established. $N_{gb}$ is the characteristic defect density of grain boundaries. Figure 3 illustrates the relationship between the defect density of $CsSnI_3$ and the grain boundary defect density under different grain sizes. Based on the reported values for both single-crystal and polycrystalline $CsSnI_3$ solar cells [24, 30], $N_{gb}$ is set to $10^{10}$ $cm^{-2}$ in this study. The grain size is modeled across a range of 0.01 μm to 100 μm, covering practical fabrication scales from nanoscale fine grains to micrometer-sized large grains [24, 56].

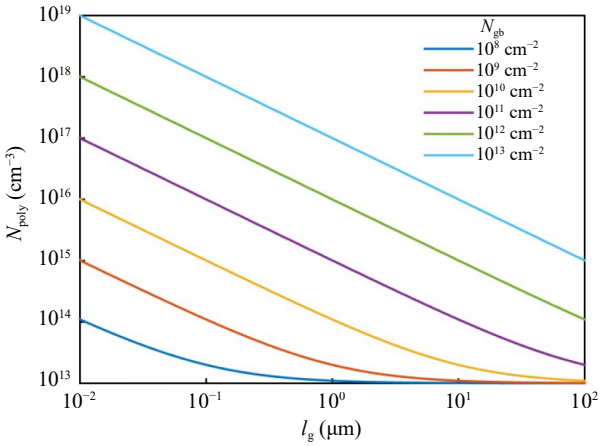



**Fig. 3** Defect density as a function of grain size in polycrystalline $CsSnI_3$ solar cells, illustrating the effect of different grain boundary defect densities ($N_{gb}$).

This Matthiessen-rule-based defect density model intuitively captures the evolution of defects in polycrystalline $CsSnI_3$: as the grain size $l_g$ decreases, the grain-boundary contribution $N_{gb}/l_g$ becomes more pronounced, leading to a substantial increase in the overall defect density $N_{poly}$; conversely, as the grain size increases, the grain-boundary effect gradually diminishes, and $N_{poly}$ approaches the intrinsic defect density of single-crystal $CsSnI_3$ $N_{mono}$. With the three key parameters — intrinsic single-crystal defect density, grain-boundary defect density, and grain size — the model quantitatively describes the influence of grain size engineering on the defect state of polycrystalline $CsSnI_3$, making it well suited for subsequent optoelectronic performance simulations and degradation mechanism analyses.

### 2.4 Mobility model

To quantify the influence of grain size on carrier mobility in polycrystalline $CsSnI_3$, the WAM is adopted in this work [57, 58]. The WAM treats the polycrystalline film as grain interiors and grain boundaries connected in series. Carriers travel sequentially through both regions, and the total transit time is the sum of the times spent in each region. The physical assumptions are: (i) grain interiors have single-crystal mobility $\mu_{mono}$; (ii) grain boundaries have a fixed thickness $l_{gb}$ and a characteristic mobility $\mu_{gb}$; (iii) other scattering mechanisms are not treated separately. The effective mobility is therefore determined by the path-length-weighted average of the reciprocal mobilities. According to the Matthiessen rule, the effective carrier mobility $\mu_{poly}$ in a polycrystalline semiconductor satisfies the reciprocal sum relationship

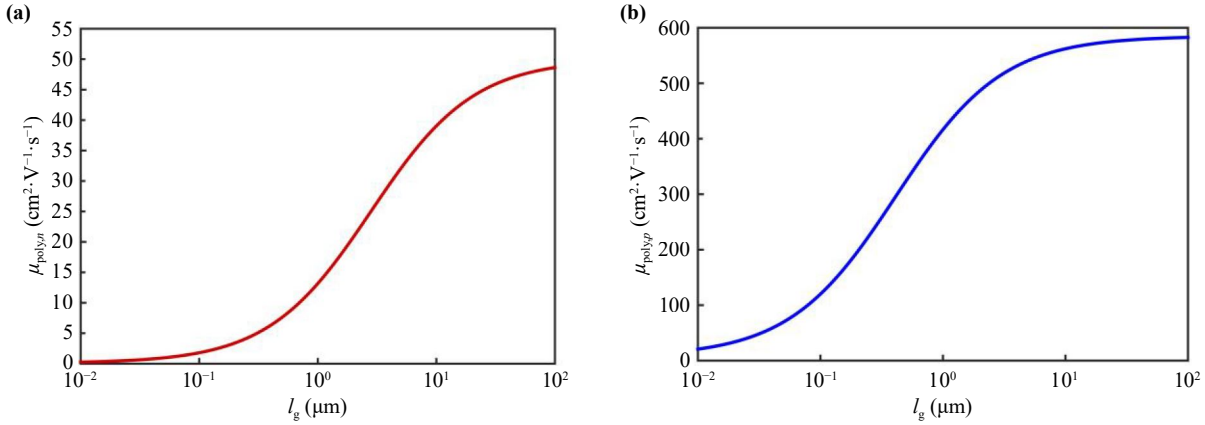



**Fig. 4** **(a)** Electron mobility and **(b)** hole mobility as a function of grain size.

with the intrinsic single-crystal mobility $\mu_{mono}$ and the grain-boundary-contributed mobility $\mu_{gb}$, as shown in Eq. (8) [19, 47]. On this basis, the effective mobility $\mu_{poly}$ of the polycrystalline material is expressed as the weighted average of the intrinsic single-crystal mobility $\mu_{mono}$ and the grain-boundary mobility $\mu_{gb}$, as given in Eq. (9) [19, 51]:

$$\frac{1}{\mu_{poly}} = \frac{1}{\mu_{mono}} + \frac{1}{\mu_{gb}}, \tag{8}$$

$$\frac{1}{\mu_{poly}} = f_g \frac{1}{\mu_{mono}} + f_{gb} \frac{1}{\mu_{gb}}, \tag{9}$$

where

$$f_g = \frac{l_g}{l_g + l_{gb}}, \quad f_{gb} = \frac{l_{gb}}{l_g + l_{gb}}, \quad f_g + f_{gb} = 1.$$

When $l_g \gg l_{gb}$, $f_g \to 1$ and $\mu_{poly} \to \mu_{mono}$. As $l_g$ decreases, $f_{gb}$ increases and grain-boundary scattering dominates. The grain boundary thickness $l_{gb}$ is set to 5 nm. Based on experimentally reported mobility data for $CsSnI_3$ single crystals and polycrystalline samples ($l_g \approx 100$ nm) [24], the electron mobilities are taken as $\mu_{mono,n} = 50$ cm$^2$·V$^{-1}$·s$^{-1}$ and $\mu_{poly,n} = 1.8$ cm$^2$·V$^{-1}$·s$^{-1}$; the hole mobilities are taken as $\mu_{mono,p} = 585$ cm$^2$·V$^{-1}$·s$^{-1}$ and $\mu_{poly,p} = 120$ cm$^2$·V$^{-1}$·s$^{-1}$. Substituting these values and $l_{gb} = 5$ nm into Eq. (9) yields the grain-boundary mobilities $\mu_{gb,n} = 0.0888$ cm$^2$·V$^{-1}$·s$^{-1}$ and $\mu_{gb,p} = 7.1$ cm$^2$·V$^{-1}$·s$^{-1}$. These values are then used to calculate $\mu_{poly}$ for grain sizes from 0.01 μm to 100 μm via Eq. (9).

Based on the fitting results, the electron and hole mobilities were calculated as a function of grain size $l_g$ ranging from 0.01 μm to 100 μm, and the results are shown in Fig. 4. It can be observed that the mobilities of both carriers increase significantly with increasing grain size when the grain size is below 10 μm. When the grain size exceeds approximately 10 μm, the mobilities gradually approach the intrinsic values of the single-crystal material, exhibiting a saturation trend. This behavior indicates that at small grain sizes, grain boundary scattering dominates the carrier transport process; as the grains grow, the grain-boundary density decreases, and the mobility progressively recovers to the intrinsic level.

The calculated defect densities and mobilities of $CsSnI_3$ for different grain sizes (0.01, 0.1, 1, 10, and 100 μm) are summarized in Table 2. At $l_g = 100$ μm, the defect density and carrier mobilities are very close to the single-crystal values, so 100 μm may be regarded as an effective single-crystalline limit in this model.

## 3 Results and discussion

Based on the mobility and defect density models, this study integrates grain-size-dependent electron mobility, hole mobility, and defect density into SCAPS simulations. A planar heterojunction device with the architecture $TiO_2$/$CsSnI_3$/Spiro-OMeTAD is established to systematically examine how device performance evolves across different grain size regimes. The investigation focuses on the effects of grain size on the optimal absorber thickness, the ideal doping concentration, and the interfacial defect tolerance, while also elucidating the coupled interdependencies among these key parameters.

### 3.1 Effect of grain size on the optimum thickness of $CsSnI_3$ absorber layer

The thickness of the absorber layer is a key performance determinant in PSCs. Increasing thickness boosts light absorption and carrier generation; however, it proportionally prolongs carrier transport, thereby intensifying recombination. For polycrystalline $CsSnI_3$, this balance is further complicated by grain-size variations, which directly modulate both mobility and defect density — and consequently, the optimal thickness itself.

This study systematically examines the effect of absorber layer thickness (over the range of 0.01–1 μm)

**Table 2** Summary table of defect densities and mobilities of $CsSnI_3$ corresponding to different grain sizes.

| $l_g$ (μm) | $N_{poly}$ ($cm^{-3}$) | $\mu_n$ ($cm^2 \cdot V^{-1} \cdot s^{-1}$) | $\mu_p$ ($cm^2 \cdot V^{-1} \cdot s^{-1}$) |
|---|---|---|---|
| 0.01 | $1.001 \times 10^{16}$ | 0.27 | 20.8 |
| 0.1 | $1.01 \times 10^{15}$ | 1.8 | 120 |
| 1 | $1.1 \times 10^{14}$ | 13.17 | 416.2 |
| 10 | $2 \times 10^{13}$ | 39.04 | 562.1 |
| 100 | $1.1 \times 10^{13}$ | 48.63 | 582.6 |

on the performance of single-crystalline $CsSnI_3$ and polycrystalline $CsSnI_3$ across grain sizes of 0.01, 0.1, 1, 10, and 100 μm. The evolution of $J_{SC}$, $V_{OC}$, FF, and PCE with these parameters is presented in Fig. 5. Based on the PCE trend, the optimal thickness exhibits a pronounced grain-size dependence. For single crystals and grain sizes of 100 μm and 10 μm, the optimal absorber thickness uniformly converges to 0.2 μm, aligning closely with the optimal range reported in prior experimental and theoretical studies on $CsSnI_3$ [9, 59]. It is indicated that when the grain size is large, the carrier transport capability is sufficient to support efficient carrier collection in a thicker absorption layer. In contrast, the optimal thickness drops to 0.1 μm for the 1 μm grain size, and further settles at 0.05 μm and 0.1 μm for grain sizes of 0.1 μm and 0.01 μm, respectively.

These results reveal that the optimal thickness decreases substantially with decreasing grain size, primarily because small-grain systems possess higher defect densities and lower carrier mobilities. As shown in the preceding calculations, when the grain size is reduced to 0.01 μm, the defect density can reach approximately $10^{16}$ $cm^{-3}$, which is far higher than the value of approximately $10^{13}$ $cm^{-3}$ for 100 μm grains. Meanwhile, grain-boundary scattering induced by smaller grain sizes significantly reduces carrier mobility, causing a pronounced shortening of the photogenerated carrier diffusion length. Under thicker-absorber conditions, photogenerated carriers are more prone to SRH nonradiative recombination before reaching the interfaces, which compromises device performance. Therefore, small-grain systems are better suited to thinner absorber layers, as this configuration shortens the carrier transport path and improves the carrier collection probability.

From a trend perspective, the open-circuit voltage drops markedly for all grain sizes when the absorber layer thickness is below roughly 0.3 μm. It is because the recombination and series resistance increases when the thickness of absorbers increases, which lowers the quasi-Fermi level splitting and consequently decreases $V_{OC}$. In contrast, for thicker layers, the voltage stabilizes and shows only a modest decrease. Once the thickness exceeds this threshold, light absorption approaches saturation, and consequently, the voltage variation becomes more gradual.

The trend of $J_{SC}$ more distinctly illustrates the influence of grain size on charge transport capability. For single-crystalline and 100 μm grains, the peak of $J_{SC}$ is observed at a thickness of 0.5 μm, beyond which it gradually diminishes with further thickening and eventually plateaus. For 10 μm grains, this peak shifts earlier to 0.4 μm, while the optimal thicknesses for 1 μm, 0.1 μm, and 0.01 μm grains are 0.2 μm, 0.1 μm, and 0.1 μm, respectively. These findings suggest that in large grains, high carrier mobility and low defect density facilitate effective long-range transport, enabling the additional photogenerated carriers from thicker absorbers to contribute efficiently to the photocurrent. Conversely, for small grains, the recombination rate outpaces the photogeneration rate as thickness increases, causing $J_{SC}$ to reach its maximum earlier and then undergo a gradual decline.

As shown in Fig. 5(c), the FF variation reveals a transport-limited behavior in devices with small grains. For all grain sizes, FF decreases markedly when the absorber thickness falls below 0.1 μm, after which the values gradually stabilize with increasing thickness. Notably, the 0.1 μm and 0.01 μm grains exhibit an extremely sharp decline in the ultra-thin thickness regime. This pronounced degradation is primarily attributed to the high density of grain boundaries, which introduces significant bulk recombination and increases series resistance within the $CsSnI_3$ layer. Although a thinner absorber shortens the carrier transport distance, the high density of grain boundaries still severely impedes carrier extraction, ultimately leading to a rapid loss in FF.

Taken together, the trends of $V_{OC}$, $J_{SC}$, FF, and PCE collectively reveal that devices with larger grains exhibit greater tolerance to thicker absorber layers, whereas reducing grain size shifts the optimal thickness markedly toward thinner regimes. Consequently, for the design of polycrystalline $CsSnI_3$ solar cells, the absorber thickness should be specifically tailored to the actual grain size in order to mitigate performance degradation arising from grain-boundary-induced recombination.

### 3.2 Effect of grain size on the optimal doping concentration in $CsSnI_3$ absorber layers

Doping concentration is a key parameter that governs

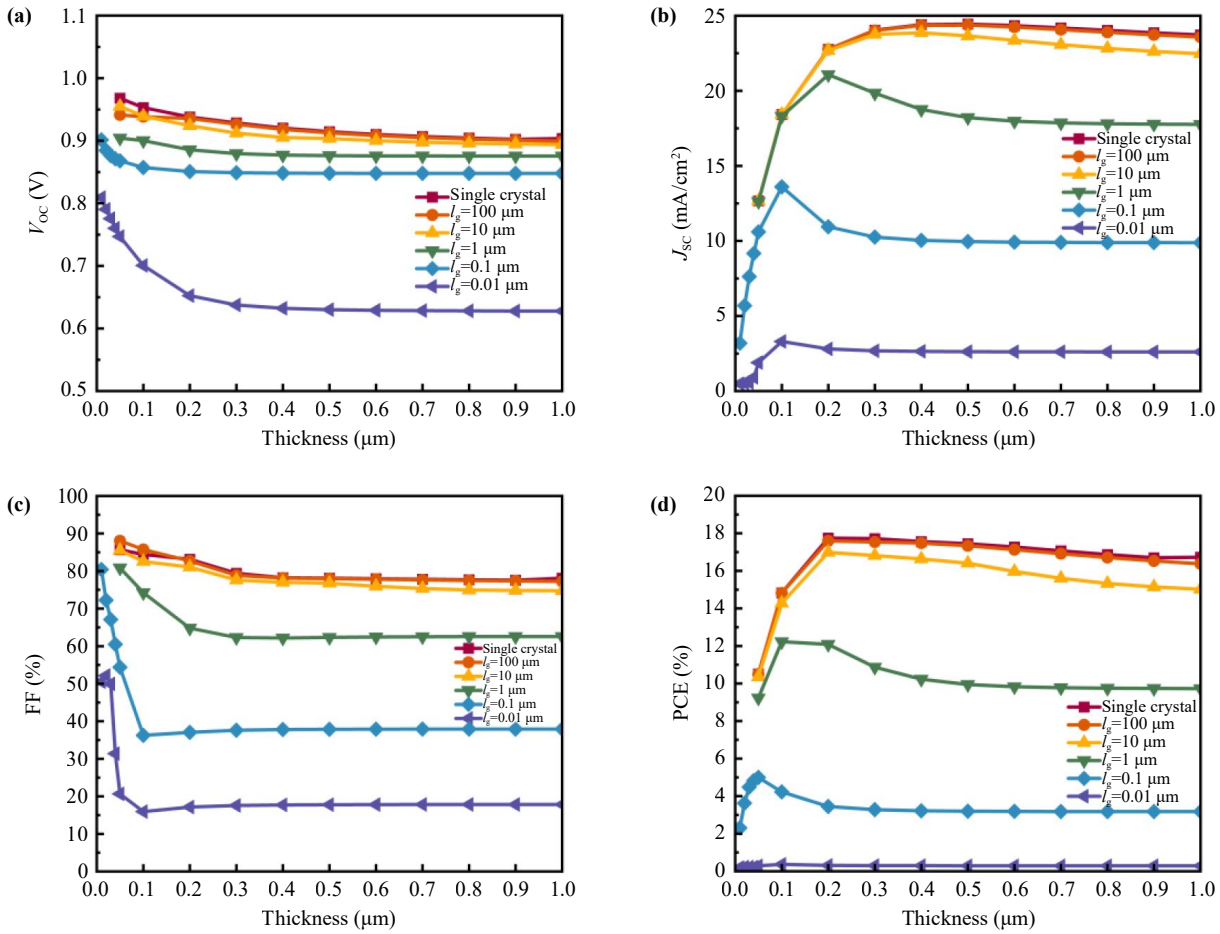



**Fig. 5** Influence of the $CsSnI_3$ absorber layer thickness on the photovoltaic performance of solar cells with different grain sizes: **(a)** $V_{OC}$, **(b)** $J_{SC}$, **(c)** FF, and **(d)** PCE. Increasing the absorber thickness initially enhances $J_{SC}$ and PCE owing to improved light harvesting, followed by performance saturation or degradation at larger thicknesses. The results further demonstrate that larger grain sizes consistently yield superior device performance because of reduced grain-boundary recombination and defect-assisted carrier losses.

charge separation, built-in electric field strength, and recombination dynamics in PSCs. A moderate increase in the acceptor doping concentration ($N_A$) within the absorber layer can enhance the built-in electric field, facilitate carrier separation, and improve the open-circuit voltage. However, excessive doping compresses the depletion region and localizes the built-in electric field near the ETL/$CsSnI_3$ interface. As a result, the field in the bulk absorber is markedly reduced, and carriers generated deep in the absorber must rely mainly on diffusion, which increases non-radiative recombination and degrades device performance. Hence, identifying the optimal doping concentration for varying grain sizes is essential for device optimization. Building on the optimal thickness determined in the preceding simulations, this study systematically investigates single-crystal $CsSnI_3$ devices alongside those with different grain sizes, over a range of $N_A$ from $10^{15}$ $cm^{-3}$ to $10^{21}$ $cm^{-3}$, which includes the unintentional doping level of $10^{17}$ $cm^{-3}$ for the single-crystal case. The corresponding results are presented in Fig. 6.

According to the PCE trends, the optimal $N_A$ exhibits a strong grain-size dependence. For single-crystalline, 100 μm, 10 μm, and 1 μm grains, the optimal doping concentration is consistently found at $5 \times 10^{18}$ $cm^{-3}$, which agrees well with the simulated value reported by Lin *et al.* [43]. In contrast, the 0.1 μm grain device achieves its peak PCE at a lower doping concentration of $1 \times 10^{18}$ $cm^{-3}$, while the finest 0.01 μm grains require a much higher concentration of $5 \times 10^{19}$ $cm^{-3}$ to reach the best performance. This non-monotonic behavior indicates that the beneficial effects of doping on carrier drift and the built-in electric field are counterbalanced by factors such as doping-induced recombination and mobility degradation, whose relative importance varies with grain size. For the 0.1 μm grains, exceeding $1 \times 10^{18}$ $cm^{-3}$ in doping concentration appears to introduce additional recombination losses. Conversely, for the extremely fine 0.01 μm grains, the exceptionally high density of grain-boundary recombination centers

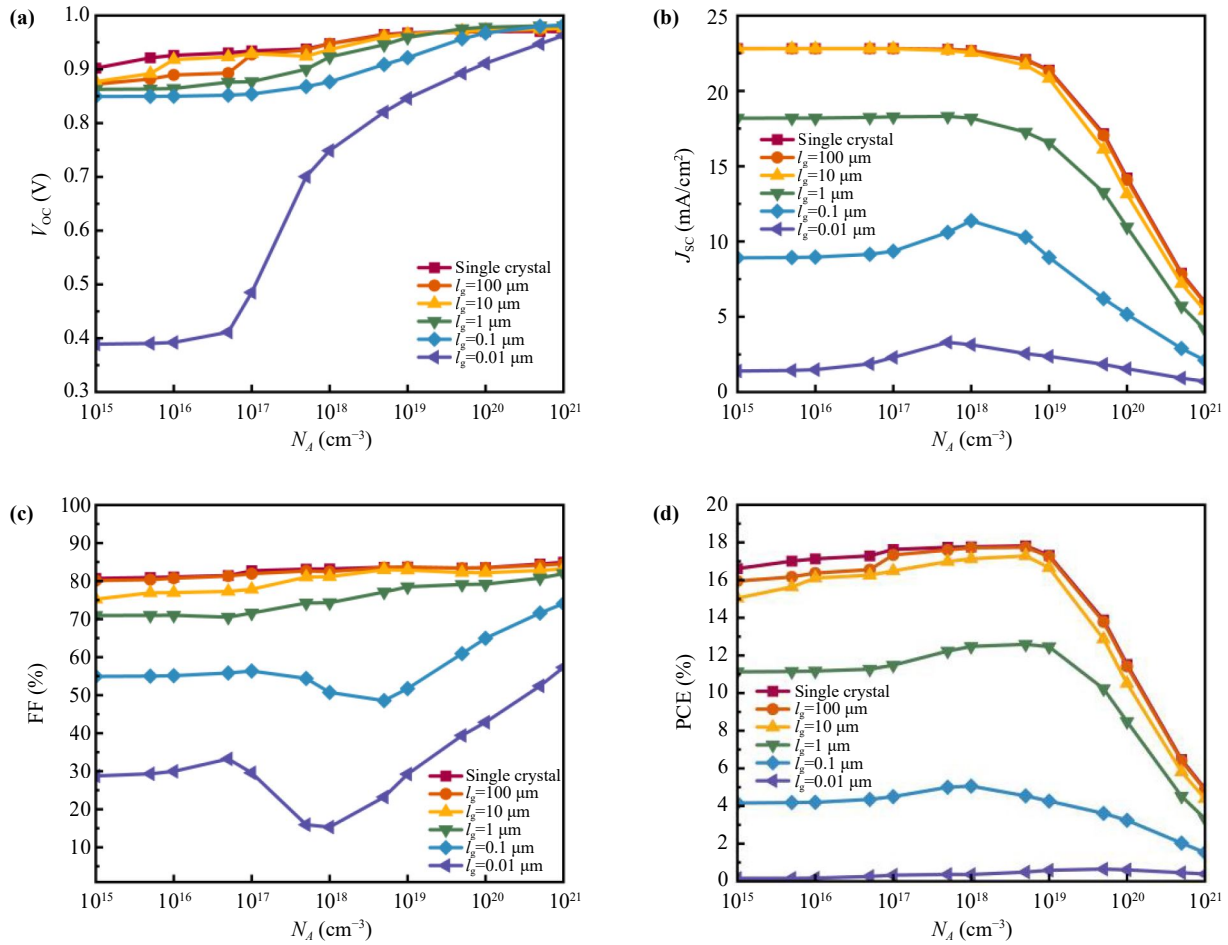



**Fig. 6** Influence of $N_A$ on the photovoltaic performance of $CsSnI_3$ PSCs with different grain sizes: **(a)** $V_{OC}$, **(b)** $J_{SC}$, **(c)** FF, and **(d)** PCE. Moderate doping enhances PCE through a strengthened built-in electric field. Excessive doping degrades performance through increased recombination. The optimal $N_A$ depends strongly on grain size. Finer grains require adjusted doping concentrations to compensate for recombination at grain boundaries.

severely limits the diffusion length; therefore, a higher doping level is necessary to enhance the built-in electric field and accelerate carrier drift transport, thereby partially suppressing the severe recombination losses. These results indicate that the optimal doping concentration should be tailored to the actual grain size.

Based on the observed $V_{OC}$ trend, the $V_{OC}$ exhibits a monotonic increase with rising doping concentration across all grain sizes. This behavior is primarily attributed to the fact that higher doping levels strengthen the built-in electric field, enhance carrier separation efficiency, and widen the quasi-Fermi level splitting, all of which collectively contribute to a sustained rise in $V_{OC}$. In contrast, $J_{SC}$ generally exhibits an initial plateau followed by a subsequent decline. Specifically, for the 0.1 μm grain size, $J_{SC}$ shows a slight increase up to $1 \times 10^{18}$ cm$^{-3}$ and then gradually decreases; for the 0.01 μm grain size, it rises moderately up to $5 \times 10^{17}$ cm$^{-3}$ and drops thereafter. This trend clearly reflects a "transport–recombination competition mechanism" prevailing in small-grain systems. At relatively low doping concentrations, the increased doping level facilitates carrier separation and collection, thereby yielding a modest improvement in $J_{SC}$. However, as the doping concentration continues to increase, the recombination probability within the device rises, and the elevated carrier concentration intensifies scattering effects, both of which collectively lead to a reduction in the photogenerated current.

Regarding the overall trend, the fill factor increases with grain size for most grain sizes. However, at the smallest grain sizes (0.1 μm and 0.01 μm), the fill factor exhibits a non-monotonic trajectory — initially rising, then declining, before recovering. This complex behavior underscores that device performance in fine-grained structures is governed by a competitive interplay between recombination losses and charge-transport limitations, rather than a single dominant mechanism, indicating a transition to multi-mechanism coupling.

Overall, as the grain size decreases, the device

becomes more sensitive to the doping concentration and requires a higher doping level to compensate for grain-boundary-induced recombination. Therefore, for high-quality large-grain $CsSnI_3$ thin films, a moderate doping concentration can yield optimal performance; whereas for small-grain systems, synergistic optimization through an enhanced built-in electric field and defect passivation is necessary to improve device performance.

### 3.3 Impact of interface defects on the performance of $CsSnI_3$ solar cells with different grain sizes

Interface defects represent a primary bottleneck for perovskite solar cell performance. In practical devices, substantial defect states inevitably emerge at both the ETL/absorber and absorber/HTL interfaces, driven by energy-level misalignment, lattice mismatch, and interfacial chemical reactions. These defects act as efficient carrier recombination centers, intensifying SRH non-radiative recombination, impairing charge extraction, and ultimately degrading the overall device performance. For polycrystalline $CsSnI_3$ solar cells, the grain size not only affects the defect distribution and carrier mobility within the absorber layer, but also alters the tolerance of the device to interface defects. This section therefore investigates the effects of interfacial defects — specifically at the ETL/$CsSnI_3$ and $CsSnI_3$/HTL junctions, as well as their synergistic variation — on device performance across different grain sizes. The aim is to further elucidate the coupling mechanism between grain size and interfacial recombination.

#### 3.3.1 Effect of ETL/$CsSnI_3$ interface defects

This study first investigates the impact of the $TiO_2$/$CsSnI_3$ interface defect density ($N_t$) on device performance. The interface defect density was varied from $10^{10}$ to $10^{17}$ $cm^{-2}$, and the simulation results are shown in Fig. 7.

Overall, the ETL/$CsSnI_3$ interface defects have a significant influence on device performance. As the interface defect density increases, the PCE shows a continuous decreasing trend for all grain sizes, indicating that this interface is an important limiting factor for device performance.

Regarding the $J_{SC}$ trend, the short-circuit current remains almost unchanged for all grain sizes, exhibiting only slight fluctuations. This suggests that the ETL/$CsSnI_3$ interface defects have a limited effect on the generation of photogenerated carriers; their primary mechanism is not reducing light absorption but rather enhancing the carrier recombination process.

By contrast, $V_{OC}$ exhibits pronounced sensitivity to interface defects. With increasing $N_t$, the $V_{OC}$ for all grain sizes decreases approximately linearly. This is because the ETL/$CsSnI_3$ interface primarily facilitates electron extraction; when the interface trap states increase, a large number of electrons are captured at the interface and undergo SRH recombination with holes, thereby significantly reducing the quasi-Fermi level splitting and ultimately causing the open-circuit voltage to decline.

The FF trend, however, exhibits a clear grain-size dependence. For single crystals and grain sizes of 100, 10, and 1 μm, FF decreases gradually with increasing interface defect density. This indicates that for high-quality thin-film systems, an increase in interface defects leads to enhanced interfacial recombination and impeded carrier transport, thereby lowering the FF. However, for grain sizes of 0.1 μm and 0.01 μm, FF exhibits an increasing trend to some extent with increasing interface defects. For devices with ultra-small grains, they inherently possess an extremely high bulk defect density (approximately $10^{15}$–$10^{16}$ $cm^{-3}$) and low mobility, and the devices are already in a recombination-limited regime. Under these circumstances, device performance is predominantly governed by bulk recombination rather than interfacial recombination.

Taken together, as the grain size decreases, the device tolerance to ETL/$CsSnI_3$ interface defects decreases significantly. Therefore, improving the grain quality and optimizing the electron extraction interface are important strategies for enhancing the performance of polycrystalline $CsSnI_3$ devices.

#### 3.3.2 Effect of $CsSnI_3$/HTL interface defects

This study also investigates the effect of varying the $CsSnI_3$/Spiro-OMeTAD interface defect density on device performance; the results are shown in Fig. 8. Compared with the ETL/$CsSnI_3$ interface, the $CsSnI_3$/HTL interface defects have a significantly weaker influence on device performance. Except for the 0.01 μm grain size, the PCE for all other grain sizes remains nearly stable when the interface defect density is below $10^{16}$ $cm^{-2}$, and begins to decrease gradually only after exceeding $10^{16}$ $cm^{-2}$. This observation indicates that the $CsSnI_3$/HTL interface possesses a high tolerance to defects. At low defect levels, holes can still be effectively extracted via Spiro-OMeTAD, resulting in minor changes in device performance. Only when the interface defect density reaches a high level does trap-assisted recombination become significantly enhanced, leading to a decline in device efficiency.

From the trend of $J_{SC}$, its variation is largely consistent with that of PCE. For most grain sizes, $J_{SC}$ remains stable before $10^{16}$ $cm^{-2}$ and then gradually declines. This suggests that HTL interface defects mainly affect the output current by reducing the carrier collection efficiency. As shown in Figs. 8(a) and (c), $V_{OC}$ and FF exhibit weak sensitivity to HTL interface defects, with only a slight decrease in the high defect range.

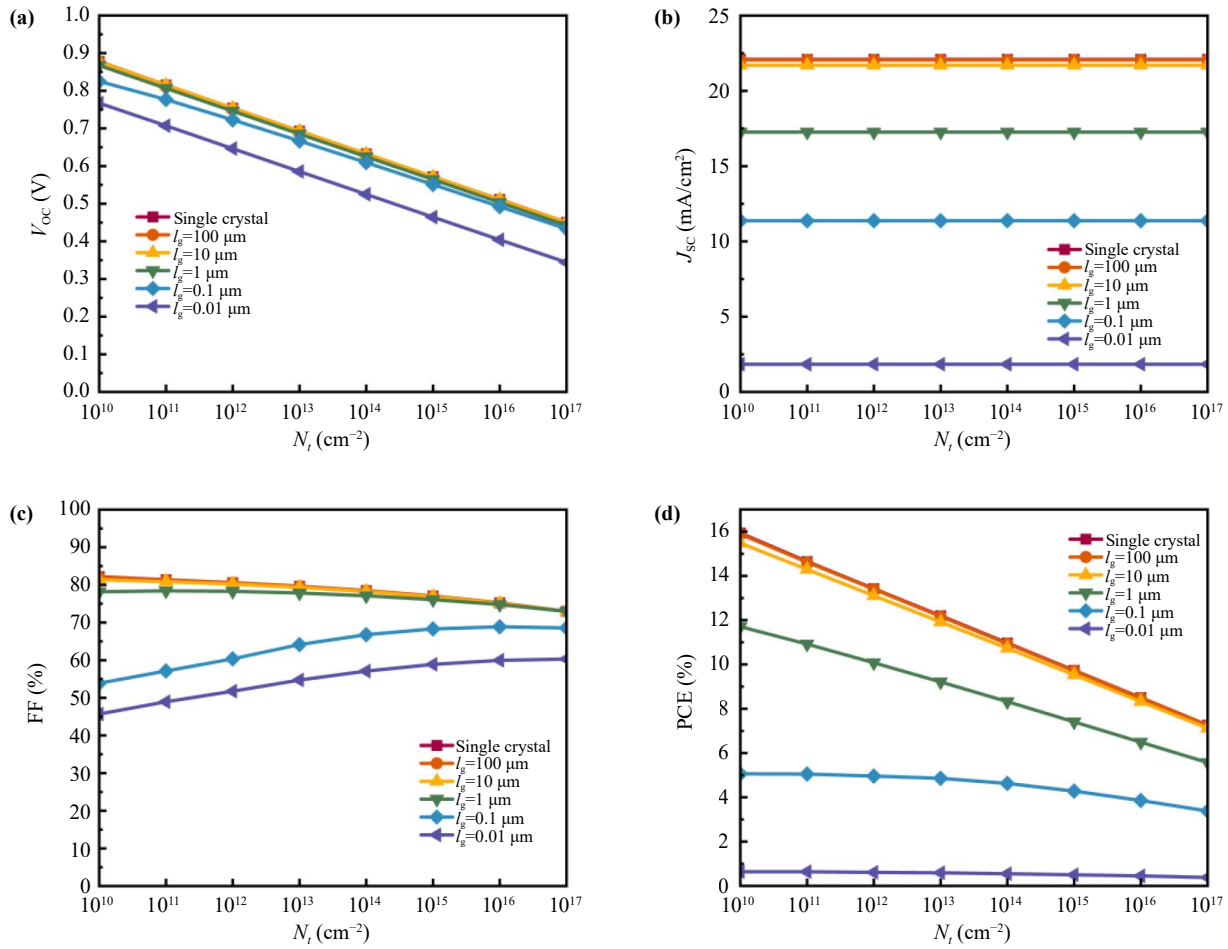



**Fig. 7** Influence of the $TiO_2/CsSnI_3$ $N_t$ on the photovoltaic performance of $CsSnI_3$ PSCs with different grain sizes: **(a)** $V_{OC}$, **(b)** $J_{SC}$, **(c)** FF, and **(d)** PCE. PCE decreases with increasing $N_t$ for all grain sizes, mainly through reduced $V_{OC}$ and variations in FF. The FF response depends on grain size: it declines for large grains but rises for ultra-small grains, where bulk recombination dominates. Smaller grains exhibit lower tolerance to interface defects, highlighting the necessity of interface quality optimization.

The more pronounced detrimental effect of ETL/$CsSnI_3$ interface defects compared with $CsSnI_3$/HTL interface defects can be understood from the band alignment and carrier recombination. The valence band offset between $CsSnI_3$ and Spiro-OMeTAD is only about 0.19 eV, which is small enough to allow efficient hole extraction. $CsSnI_3$ is p-type. The pronounced asymmetry in defect tolerance between the ETL/$CsSnI_3$ and $CsSnI_3$/HTL interfaces may also be qualitatively rationalized within the AMIP (atomic mean inner potential)-based electronegativity framework: the atomic constituents across the ETL/$CsSnI_3$ interface may exhibit a larger electrostatic potential mismatch than those across the $CsSnI_3$/HTL interface, which could contribute to a stronger tendency for electron capture at the ETL side [60]. At the ETL/$CsSnI_3$ interface, defects mainly act as electron traps. An increase in interface defect density significantly shortens the electron lifetime and reduces the quasi-Fermi level splitting, causing a pronounced decrease in $V_{OC}$ and PCE. In contrast, at the $CsSnI_3$/HTL interface, defects mainly capture holes. The device is less sensitive to hole capture, so the HTL interface exhibits a higher defect tolerance.

### 3.3.3 Synergistic simulation analysis of defects at both interfaces

To further investigate the coupling effect of recombination at both interfaces, we simultaneously varied the defect densities at the ETL/$CsSnI_3$ and $CsSnI_3$/HTL interfaces and analyzed the resulting device performance, the results are presented in Fig. 9.

Under the synergistic variation of defects at both interfaces, the trends of PCE, $V_{OC}$, and FF are highly consistent with those obtained for varying ETL/$CsSnI_3$ interface defects, whereas the $J_{SC}$ trend is more closely aligned with that observed at the $CsSnI_3$/HTL interface.

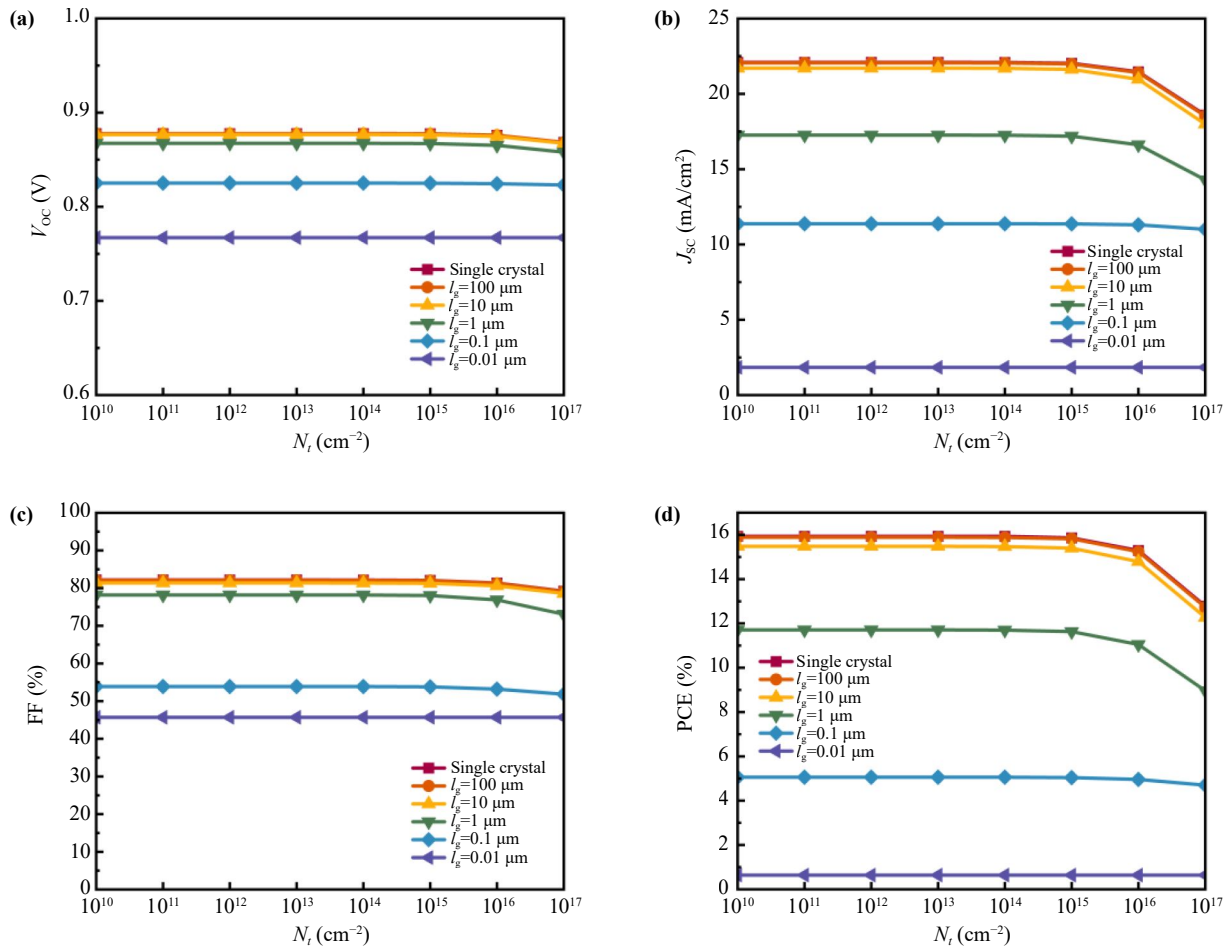



**Fig. 8** Influence of the $CsSnI_3$/Spiro-OMeTAD $N_t$ on the photovoltaic performance of $CsSnI_3$ PSCs with different grain sizes: **(a)** $V_{OC}$, **(b)** $J_{SC}$, **(c)** FF, and **(d)** PCE. For most grain sizes, PCE and $J_{SC}$ remain stable below $10^{16}$ cm$^{-3}$ and decline only at higher defect densities; $V_{OC}$ and FF show weak sensitivity throughout. This interface exhibits high defect tolerance relative to the ETL/absorber interface, indicating that hole extraction is less affected by interfacial recombination.

The above results further demonstrate that interface optimization in $CsSnI_3$ solar cells should prioritize ETL/$CsSnI_3$ interface passivation, complemented by improvements at the HTL side, to achieve synergistic optimization.

### 3.4 Decoupling analysis of mobility and defect density contributions

To clarify the physical origin of how grain size affects device performance, this section performs decoupling simulations under a unified reference structure. The absorber thickness is fixed at 0.2 μm, the acceptor concentration at $5 \times 10^{18}$ cm$^{-3}$, and no interface defects are included. Four conditions are set: (i) single-crystal baseline (simulated only once); (ii) mobility-only variation, with defect density fixed at the single-crystal value; (iii) defect-only variation, with mobility fixed at the single-crystal value; (iv) coupled variation, with both set to the corresponding polycrystalline values for each grain size (see Table 2).

When only mobility varies, $V_{OC}$ hardly changes with grain size and remains close to the single-crystal baseline, as shown in Fig. 10(a). This may be because when the defect density remains at the single-crystal level, SRH non-radiative recombination is very weak, so $V_{OC}$ is insensitive to mobility. When only defect density varies, $V_{OC}$ decreases as grain size decreases, indicating that defect-assisted recombination may be the main cause of voltage loss. In the coupled model, $V_{OC}$ decreases further, suggesting possible synergistic degradation.

As seen in Figs. 10(b) and (c), the mobility-only and defect-only curves are relatively close, indicating that their effects on $J_{SC}$ and FF are comparable. This may be because increased defect density also shortens carrier lifetime and reduces collection efficiency, while decreased mobility directly limits transport; both significantly degrade current and fill factor at small grain sizes. In the coupled model, $J_{SC}$ and FF decrease further with decreasing grain size and are much lower than those

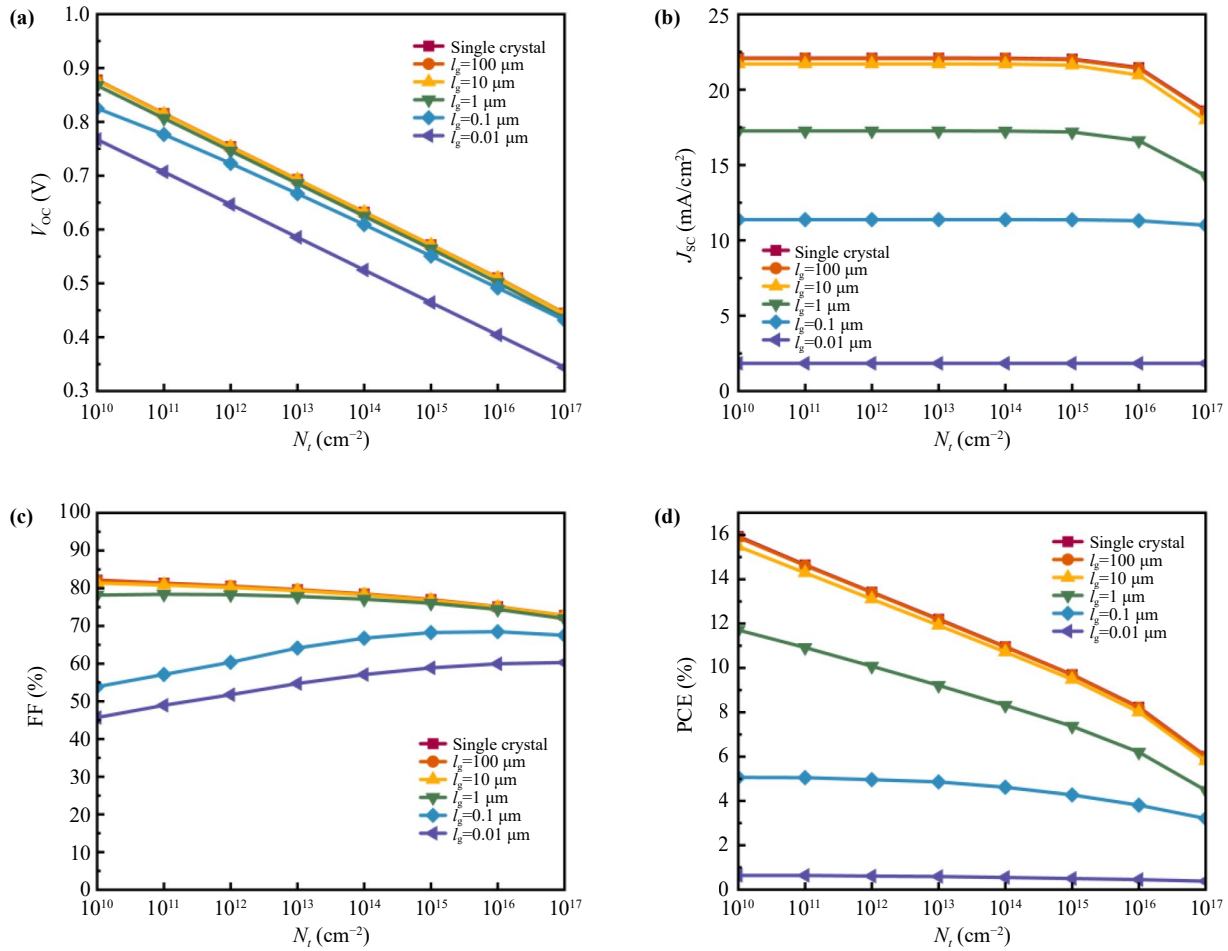



**Fig. 9** Influence of simultaneous variation of defect densities at both the ETL/$CsSnI_3$ and $CsSnI_3$/HTL interfaces on the photovoltaic performance of $CsSnI_3$ PSCs with different grain sizes: **(a)** $V_{OC}$ **(b)** $J_{SC}$, **(c)** FF, and **(d)** PCE. The trends of PCE, $V_{OC}$ and FF are consistent with those observed for ETL/ $CsSnI_3$ interface defects, while the $J_{SC}$ trend follows that of $CsSnI_3$/HTL interface defects. These results indicate that interface optimization should prioritize passivation of the ETL/ $CsSnI_3$ interface, with complementary improvements at the HTL side.

from single-variable variations, indicating that the coupling of the two may cause severe transport and recombination losses at small grain sizes.

As shown in Fig. 10(d), the single-crystal baseline PCE is 17.82%. The mobility-only and defect-only cases decrease to 4.84% and 4.09% at 0.01 μm, respectively, with comparable loss magnitudes, indicating that in the small-grain region, both mobility degradation and defect recombination cannot be ignored in PCE loss. The coupled model gives a PCE of only 0.41%, much lower than either the mobility-only or defect-only case, indicating a pronounced synergistic effect. When grain size increases to 10 μm and 100 μm, the mobility-only, defect-only, and coupled curves gradually approach the single-crystal baseline, and the grain-boundary effect is significantly weakened.

In summary, the decoupling analysis shows that defect-assisted recombination plays a dominant role in reducing $V_{OC}$, while $J_{SC}$ and FF are sensitive to both mobility and defect density, with comparable contributions. At small grain sizes, their synergy leads to a sharp drop in PCE. Therefore, the grain-size dependence may be a physical result of both grain-boundary scattering and defect recombination. For small-grain devices, both carrier mobility and bulk defect recombination need to be improved simultaneously; for large-grain devices, the bulk parameters are already close to single-crystal levels, and further performance improvement may mainly rely on interface defect passivation and interface energy-level matching optimization.

## 4 Conclusions

In this work, we develop a quantitative model linking grain size to carrier mobility and defect density, based on the weighted average method and Matthiessen's rule. Using SCAPS-1D numerical simulations, we systematically investigate how grain size influences the performance of $TiO_2$/$CsSnI_3$/Spiro-OMeTAD perovskite solar cells. Our

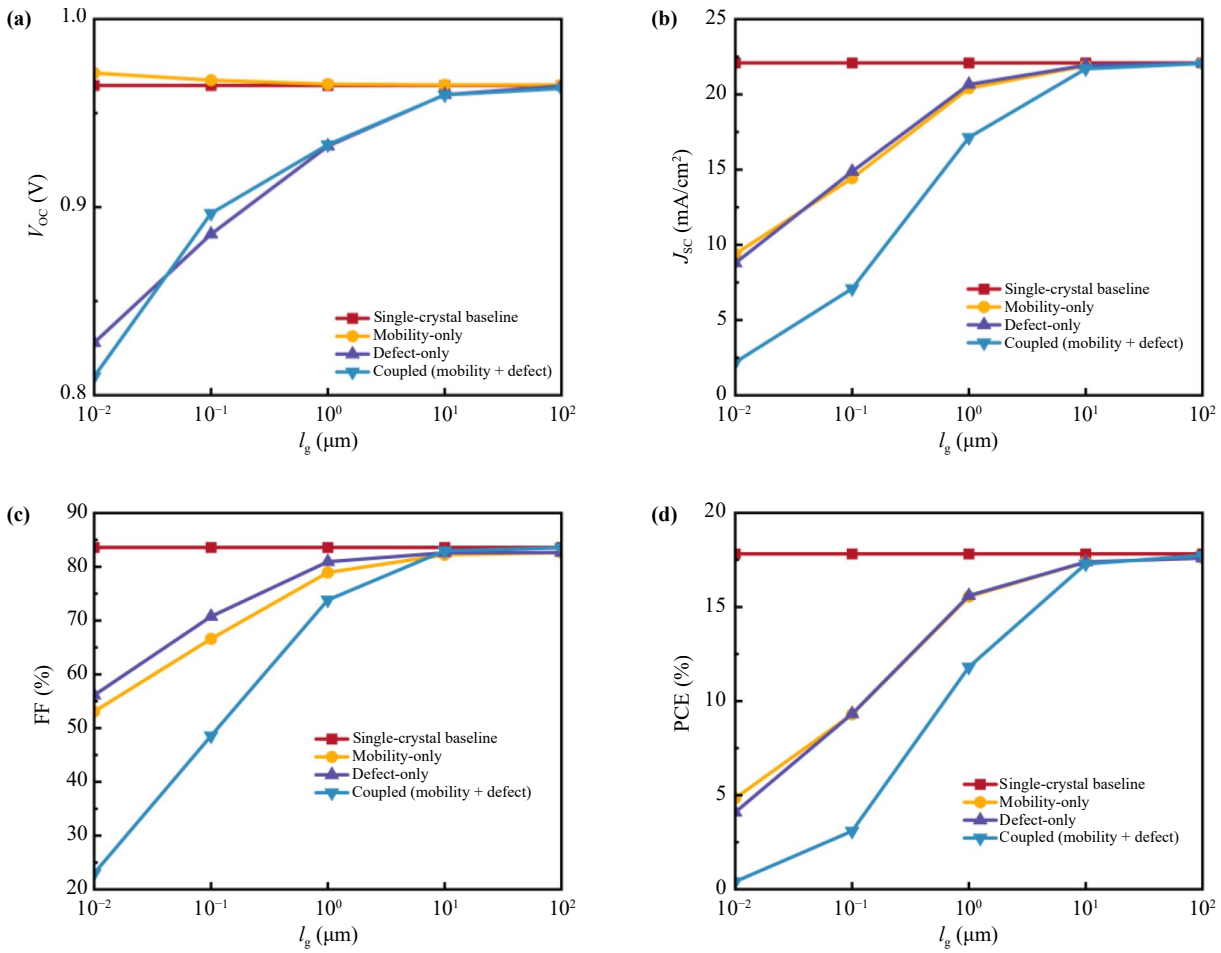



**Fig. 10** Decoupled effects of mobility and defect density on the photovoltaic performance of $CsSnI_3$ PSCs with different grain sizes. **(a)** $V_{OC}$, **(b)** $J_{SC}$, **(c)** FF, and **(d)** PCE as a function of grain size. Lines are guides to the eye only. All simulations adopt a unified reference structure (absorber thickness 0.2 μm, $N_A = 5 \times 10^{18}$ cm$^{-3}$, no interface defects) to isolate the contributions of bulk mobility and bulk defect density.

analysis focuses on the modulating effects of absorber thickness, acceptor doping concentration, and interface defects on devices with varying grain sizes, leading to some key findings:

As the grain size increases, both electron and hole mobilities improve significantly while the defect density decreases markedly. At a grain size of 100 μm, the electron and hole mobilities reach 48.63 and 582.6 cm$^2$·V$^{-1}$·s$^{-1}$, respectively, and the defect density drops to approximately $1.1 \times 10^{13}$ cm$^{-3}$.

Grain size significantly influences the optimal absorber thickness of $CsSnI_3$. For single-crystalline, 100 μm, and 10 μm grains, the optimal thickness remains 0.2 μm, yielding PCEs of 17.75% ($V_{OC}$ = 0.9379 V, $J_{SC}$ = 22.76 mA/cm$^2$, FF = 83.14%), 17.60% (0.9356 V, 22.76 mA/cm$^2$, 82.67%), and 16.99% (0.9241 V, 22.68 mA/cm$^2$, 81.06%), respectively. As the grain size decreases to 1 μm, 0.1 μm, and 0.01 μm, the optimal thickness shifts markedly to 0.1 μm, 0.05 μm, and 0.1 μm, with corresponding PCEs of 12.23% (0.9001 V, 18.31 mA/cm$^2$, 74.24%), 5.00% (0.8679 V, 10.60 mA/cm$^2$, 54.39%), and 0.37% (0.7006 V, 3.30 mA/cm$^2$, 15.94%).

Grain size also plays a critical role in determining the optimal doping concentration. For single-crystalline, 100 μm, 10 μm, and 1 μm grains, the optimal acceptor doping concentration is consistently $5 \times 10^{18}$ cm$^{-3}$, yielding peak PCEs of 17.82% ($V_{OC}$ = 0.9647 V, $J_{SC}$ = 22.09 mA/cm$^2$, FF = 83.61%), 17.75% (0.9631 V, 22.06 mA/cm$^2$, 83.57%), 17.29% (0.9597 V, 21.71 mA/cm$^2$, 82.98%), and 12.59% (0.9458 V, 17.26 mA/cm$^2$, 77.11%), respectively. In contrast, the 0.1 μm grains exhibit an optimal concentration of $1 \times 10^{18}$ cm$^{-3}$, achieving a PCE of 5.06% (0.8766 V, 11.37 mA/cm$^2$, 50.72%), while the finest 0.01-μm grains require a higher concentration of $5 \times 10^{19}$ cm$^{-3}$, with a PCE of 0.65% (0.8924 V, 1.84 mA/cm$^2$, 39.4%). These trends correlate performance degradation with reduced mobility and enhanced recombination in finer grains.

The ETL/$CsSnI_3$ interface defects have a considerably

stronger impact on device performance than the $CsSnI_3$/HTL interface defects. With increasing ETL side interface defects, $V_{OC}$ decreases approximately linearly and PCE declines continuously, whereas HTL interface defects show significant influence only in the high defect density region. Synergistic simulations of both interfaces further demonstrate that the ETL/$CsSnI_3$ interface dominates the variation of $V_{OC}$, FF, and PCE, while the $CsSnI_3$/HTL interface affects $J_{SC}$ more prominently.

Overall, grain size is a critical structural determinant of $CsSnI_3$ perovskite solar cell performance. It governs carrier mobility and defect density, which in turn dictate the optimal thickness, doping level, and interface tolerance. Larger grains thus enable higher efficiency, a broader optimization window. This study provides a theoretical foundation and simulation-based guidance for the structural optimization and design of high-performance lead-free polycrystalline $CsSnI_3$ perovskite solar cells. Extending the present device-level analysis to include fundamental electronegativity descriptors — such as the AMIP-based scale, which bridges atomic-scale electrostatic properties and macroscopic defect behavior — could provide a more predictive framework for grain-boundary engineering in lead-free perovskites [60]. It should be noted that this work focuses on steady-state device performance, and long-term operational stability, including degradation, thermal cycling, and ion migration, was not simulated. These aspects will be investigated in future work.

**Declarations** The authors declare that they have no competing interests and there are no conflicts.

**Acknowledgements** This work was supported by the National Natural Science Foundation of China (NSFC) (No. 12374075) and the Zhangzhou Natural Science Foundation (No. ZZ2025JH27). The authors gratefully acknowledge the SCAPS-1D research team for providing the SCAPS-1D simulation software.

## References

1. NLR, Best research-cell efficiency chart, URL: www.nlr.gov/pv/cell-efficiency
2. W. Q. Yang, X. Y. Yang, R. Su, Y. Y. Feng, L. C. Zhao, M. C. Li, X. Q. Wang, R. Zhu, C. F. Pan, and D. Y. Luo, System-level integration of halide perovskite optoelectronics for its commercial deployment, *Nat. Commun.* 17(1), 5076 (2026)
3. H. S. Kim, J. W. Lee, A. Hagfeldt, M. Grätzel, and N. G. Park, Molecular-level understandings and device strategies for $FAPbI_3$-based perovskite solar cells, *Chem. Soc. Rev.* 54(23), 11061 (2025)
4. P. Barua, N. K. Elumalai, A. Uddin, P. Sonar, and K. Krishnan, Stability of lead-free perovskite solar cells, *Adv. Sustain. Syst.* 10(3), e00008 (2026)
5. L. P. Duan and A. Uddin, Defects and stability of perovskite solar cells: a critical analysis, *Mater. Chem. Front.* 6(4), 400 (2022)
6. A. S. Abdulkarim, M. Srivastava, T. Ngulezhu, D. Singh, K. Strzałkowski, R. C. Singh, M. Z. A. Yahya, S. N. F. Yusuf, and M. Diantoro, An overview of tin based perovskite solar cells: Stability and efficiency, *Curr. Appl. Phys.* 71, 190 (2025)
7. I. Chung, J. H. Song, J. Im, J. Androulakis, C. D. Malliakas, H. Li, A. J. Freeman, J. T. Kenney, and M. G. Kanatzidis, $CsSnI_3$: Semiconductor or metal? High electrical conductivity and strong near-infrared photoluminescence from a single material. High hole mobility and phase-transitions, *J. Am. Chem. Soc.* 134(20), 8579 (2012)
8. M. Azadinia, M. Ameri, R. T. Ghahrizjani, and M. Fathollahi, Maximizing the performance of single and multijunction MA and lead-free perovskite solar cell, *Mater. Today Energy* 20, 100647 (2021)
9. S. Lin, B. P. Zhang, T. Y. Lü, J. C. Zheng, H. Q. Pan, H. T. Chen, C. J. Lin, X. R. Li, and J. R. Zhou, Inorganic lead-free B-γ-$CsSnI_3$ perovskite solar cells using diverse electron-transporting materials: A simulation study, *ACS Omega* 6(40), 26689 (2021)
10. H. Z. Xu, Z. C. Guo, P. Chen, and S. C. Wang, Toward durable all-inorganic perovskite solar cells: from lead-based to lead-free, *Chem. Commun.* 60(85), 12287 (2024)
11. H. X. Yu, L. J. Fu, T. Y. Sun, D. Y. Wang, Z. R. Liu, et al., Modulation of electron transport layers to minimize voltage loss in $CsSnI_3$ perovskite solar cells, *ACS Energy Lett.* 10(6), 2889 (2025)
12. Y. F. Wu, W. B. Chu, A. S. Vasenko, and O. V. Prezhdo, Common defects accelerate charge carrier recombination in $CsSnI_3$ without creating mid-gap states, *J. Phys. Chem. Lett.* 12(36), 8699 (2021)
13. P. Xu, S. Y. Chen, H. J. Xiang, X. G. Gong, and S. H. Wei, Influence of defects and synthesis conditions on the photovoltaic performance of perovskite semiconductor $CsSnI_3$, *Chem. Mater.* 26(20), 6068 (2014)
14. L. T. Dai, W. R. Chen, Q. M. Geng, Y. Xu, G. W. Zhou, N. Chen, and X. J. Li, Reductive contact and dipolar interface engineering enable stable flexible $CsSnI_3$ nanowire photodetectors, *Nanoscale* 18(24), 13051 (2026)
15. L. Z. Cao, X. Liu, Y. D. Li, X. S. Li, L. N. Du, S. Y. Chen, S. L. Zhao, and C. Wang, Recent progress in all-inorganic metal halide nanostructured perovskites: Materials design, optical properties, and application, *Front. Phys. (Beijing)* 16(3), 33201 (2021)
16. X. X. Hao, X. Q. Chen, X. Zhou, L. Zhang, J. H. Tao, C. H. Wang, T. Wu, and W. Dai, Performance optimization for PbTe-based thermoelectric materials, *Front. Energy Res.* 9, 754532 (2021)
17. B. Xu, T. F. Gao, J. D. Yuan, X. Jin, P. J. Zhang, S. W. Xue, D. Wang, X. P. Liu, W. F. Zhao, and Q. H. Li, Unraveling the origin of Mn(II) near-infrared luminescence via crystal field engineering, *Laser Photonics Rev.* 20(17), e71288 (2026)
18. B. Li, H. X. Di, B. H. Chang, R. Y. Yin, L. Fu, Y. N. Zhang, and L. W. Yin, Efficient passivation strategy on Sn related defects for high performance all-inorganic $CsSnI_3$ perovskite solar cells, *Adv. Funct. Mater.* 31(11),

2007447 (2021)
19. B. Olyaeefar, S. Ahmadi-Kandjani, and A. Asgari, Classical modelling of grain size and boundary effects in polycrystalline perovskite solar cells, *Sol. Energy Mater. Sol. Cells* 180, 76 (2018)
20. Y. Yin, X. Y. Shen, Q. D. Sun, H. Yang, and Y. Y. Cao, Termination-determined defect tolerance in $CsPbI_3$: a first-principles guide for surface defect engineering, *Comput. Mater. Sci.* 274, 115042 (2026)
21. L. Zhang, Q. Wang, J. Li, and C. H. Wang, The role of ZnO as a dopant and an intergranular phase in the electrical properties of $Ca_{0.6}Sr_{0.4}TiO_3$ Ceramics, *Front. Energy Res.* 9, 807300 (2021)
22. J. X. Xu, Y. Wang, S. D. Huo, Q. J. Tian, Y. H. Wang, et al., Monolithic 2D synapse-neuron integration via defect-engineered h-BN for energy-efficient neuromorphic computing, *Adv. Funct. Mater.* 36(69), e77333 (2026)
23. S. Q. Luo, J. F. Wang, B. Yang, and Y. B. Yuan, Recent advances in controlling the crystallization of two-dimensional perovskites for optoelectronic device, *Front. Phys. (Beijing)* 14(5), 53401 (2019)
24. B. Wu, Y. Y. Zhou, G. C. Xing, Q. Xu, H. F. Garces, A. Solanki, T. W. Goh, N. P. Padture, and T. C. Sum, Long minority-carrier diffusion length and low surface-recombination velocity in inorganic lead-free $CsSnI_3$ perovskite crystal for solar cells, *Adv. Funct. Mater.* 27(7), 1604818 (2017)
25. Q. Z. An, F. Paulus, D. Becker-Koch, C. Cho, Q. Sun, A. Weu, S. Bitton, N. Tessler, and Y. Vaynzof, Small grains as recombination hot spots in perovskite solar cells, *Matter* 4(5), 1683 (2021)
26. M. H. Zhang, K. L. Chen, Y. X. Wei, W. Z. Hu, Z. Y. Cai, et al., Strategies for optimizing the morphology of $CsSnI_3$ perovskite solar cells, *Crystals* 13(3), 410 (2023)
27. R. T. Prabu, S. R. Malathi, R. Kumar, H. S. Alkhalidi, and A. Kumar, Impact of grain size and grain nature in thin-film solar cells, *Energy Technol.* 12(1), 2300754 (2024)
28. S. Y. Ye, Y. Chen, H. B. Wu, H. T. Lang, H. Wang, et al., Heterodimensional epitaxy of $CsSnI_3$ microcrystalline cubes for bright and efficient near-infrared light-emitting diode, *Adv. Mater.* 38(6), e12927 (2026)
29. J. M. Li, J. T. Huang, A. D. Zhao, Y. F. Li, and M. D. Wei, An inorganic stable Sn-based perovskite film with regulated nucleation for solar cell application, *J. Mater. Chem. C* 8(26), 8840 (2020)
30. Q. Sun, A. J. Gu, H. X. Yu, Y. Shen, and M. K. Wang, A single crystal derived precursor for improving the performance of $CsSnI_3$ perovskite solar cells, *J. Mater. Chem. A* 11(32), 17292 (2023)
31. J. Yi, Y. X. Zhan, Y. M. Hu, S. Zhao, and H. H. Li, Machine learning force fields for inorganic crystalline materials: principles, advances, and emerging applications, *Phys. Chem. Chem. Phys.* 28(30), 18284 (2026)
32. J. X. Wei, F. R. Liang, H. Feng, and L. Ran, Condition monitoring of discrete power devices: a data-driven approach with stress quantification and mold temperature sensing, *IEEE J. Emerg. Sel. Top. Power Electron.* 12(3), 2569 (2024)
33. Y. Ping, Y. Z. He, Q. Y. Li, J. Zhang, S. B. She, Z. J. Zhang, Y. Wang, and S. L. Huang, Junction temperature estimation of SiC MOSFETs based on mechanical stress waves and Gaussian process regression, *IEEE Trans. Power Electron*, doi: 10.1109/TPEL.2026.3723564
34. G. D. Li, M. X. Xu, and Q. W. Bai, Computation simulation of stable perovskite solar cells with quasi-2D/2D bilayer for exceeding 30% efficiency, *Front. Phys. (Beijing)* 21(10), 104201 (2026)
35. M. Burgelman, P. Nollet, and S. Degrave, Modelling polycrystalline semiconductor solar cells, *Thin Solid Films* 361–362, 527 (2000)
36. M. Burgelman, K. Decock, S. Khelifi, and A. Abass, Advanced electrical simulation of thin film solar cells, *Thin Solid Films* 535, 296 (2013)
37. S. Degrave, M. Burgelman, and P. Nollet, Modelling of polycrystalline thin film solar cells: new features in SCAPS Version 2.3, Proceedings of the 3rd World Conference on Photovoltaic Energy Conversion. Osaka, Japan: IEEE, 2003, page 487
38. E. H. Ihalane, L. Atourki, H. Kirou, A. Ihlal, and K. Bouabid, Numerical study of thin films CIGS bilayer solar cells using SCAPS, *Mater. Today Proc.* 3(7), 2570 (2016)
39. R. T. Mouchou, T. C. Jen, O. T. Laseinde, and K. O. Ukoba, Numerical simulation and optimization of p-$NiO$/n-$TiO_2$ solar cell system using SCAPS, *Mater. Today Proc.* 38(Part 2), 835 (2021)
40. Q. Fatima, A. A. Haidry, R. Hussain, and H. Q. Zhang, Device simulation of a thin-layer $CsSnI_3$-based solar cell with enhanced 31.09% efficiency, *Energy Fuels* 37(10), 7411 (2023)
41. M. K. Hossain, M. S. Uddin, G. F. I. Toki, M. K. A. Mohammed, R. Pandey, et al., Achieving above 24% efficiency with non-toxic $CsSnI_3$ perovskite solar cells by harnessing the potential of the absorber and charge transport layers, *RSC Adv.* 13(34), 23514 (2023)
42. V. H. D. Araújo, A. F. Nogueira, J. C. Tristão, and L. J. D. Santos, Advances in lead-free perovskite solar cell design via SCAPS-1D simulations, *RSC Sustain.* 3(10), 4314 (2025)
43. S. Lin, B. P. Zhang, W. C. Wang, T. Y. Lü, J. R. Zhou, X. Y. Li, Y. H. Fang, and J. C. Zheng, Simulation study on the all-inorganic $CsSn_xGe_{1-x}I_3$-based perovskite solar cells using isotypic perovskites as hole transport layers, *Energy Fuels* 38(20), 19831 (2024)
44. T. B. Song, T. Yokoyama, C. C. Stoumpos, J. Logsdon, D. H. Cao, M. R. Wasielewski, S. Aramaki, and M. G. Kanatzidis, Importance of reducing vapor atmosphere in the fabrication of tin-based perovskite solar cells, *J. Am. Chem. Soc.* 139(2), 836 (2017)
45. M. Mahiny, S. Ahmadi-Kandjani, and B. Olyaeefar, Classical modeling of extrinsic degradation in polycrystalline perovskite solar cells; defect induced degradation, *Sol. Energy Mater. Sol. Cells* 261, 112500 (2023)
46. A. J. McEvoy, T. Markvart, and L. Castañer, Solar Cells: Materials, Manufacture and Operation, 2nd Ed., Oxford: Elsevier, 2012
47. S. Kasap and P. Capper, Springer Handbook of Electronic and Photonic Materials, 2nd Ed., Cham: Springer, 2017
48. I. Pelant and J. Valenta, Luminescence Spectroscopy of Semiconductors, Oxford: Oxford University Press, 2012
49. R. F. Pierret, Semiconductor Device Fundamentals,

Reading: Addison-Wesley, 1996
50. P. K. Nayak, S. Mahesh, H. J. Snaith, and D. Cahen, Photovoltaic solar cell technologies: Analysing the state of the art, *Nat. Rev. Mater.* 4(4), 269 (2019)
51. S. A. Dar, and B. S. Sengar, Analytical modeling and numerical investigation of grain size effects on polycrystalline perovskite based thin-film solar cells: Performance insights and implications, *Sol. Energy* 289, 113313 (2025)
52. T. O. Ahmed, T. T. Ibrahim, E. O. Oladimeji, and J. D. Koffa, An absorber enrichment study and implications on the performance of lead-free $CsSnI_3$ perovskite solar cells (PSCs) using one-dimensional solar cell capacitance simulator (1D-SCAPS), *Braz. J. Phys.* 54(2), 42 (2024)
53. S. Ullah, Q. ul Ain, S. Qamar, F. Khan, and M. T. Khan, Achieving beyond 30% efficiency for hole-transport-layer-free $CsSnI_3$ perovskite solar cell: A comprehensive simulation study, *Phys. Scr.* 99(10), 105998 (2024)
54. S. Bansal, and P. Aryal, Evaluation of new materials for electron and hole transport layers in perovskite-based solar cells through SCAPS-1D simulations. Proceedings of the 2016 IEEE 43rd Photovoltaic Specialists Conference, Portland: IEEE, 2016, page 747
55. H. Rajasekaran, T. Vasudevan, and L. C. Chen, Numerical investigation of high-performance bilayer tin-based perovskite solar cells with SCAPS-1D, *Mater. Adv.* 7(3), 1884 (2026)
56. H. X. Yu, Z. G. Zhang, H. L. Dong, X. J. Li, Z. R. Liu, J. Y. Huang, Y. Q. Fu, Y. Shen, and M. K. Wang, Inorganic $CsSnI_3$ perovskite solar cells with an efficiency above 13.6%, *ACS Energy Lett.* 9(12), 5870 (2024)
57. S. Wo, R. L. Headrick, and J. E. Anthony, Fabrication and characterization of controllable grain boundary arrays in solution-processed small molecule organic semiconductor films, *J. Appl. Phys.* 111(7), 073716 (2012)
58. F. V. Farmakis, J. Brini, G. Kamarinos, C. T. Angelis, C. A. Dimitriadis, and M. Miyasaka, On-current modeling of large-grain polycrystalline silicon thin-film transistors, *IEEE Trans. Electron Devices* 48(4), 701 (2001)
59. M. A. Khatun, A. Imam, S. Mustak, and R. Mia, Numerical simulation and optimization of $CsPbI_3/CsSnI_3$ dual-absorber solar cells: Effects of thickness and defect densities using SCAPS 1D, *Next Energy* 11, 100554 (2026)
60. J. C. Zheng, First-principles electronegativity scale from the atomic mean inner potential, *Front. Phys. (Beijing)* 21(11), 114201 (2026)